Industrial Chemistry & Materials

ROYAL SOCIETY OF CHEMISTRY

PAPER

View Article Online
View Journal | View Issue

Cite this: *Ind. Chem. Mater.*, 2025, **3**, 475

Nitrogen doped hierarchical porous carbon for supercapacitors and zinc ion hybrid capacitors†

Jun Ni,[a] Weijian Chen,[a] Xinyang Zhang,[a] Hui Xu,[a] Minghui Zhang*[b] and Xiaoliang Wu *[a]

Received 31st March 2025,
Accepted 17th June 2025

DOI: 10.1039/d5im00044k

rsc.li/icm

Heteroatom-doped hierarchical porous carbon materials demonstrate significant promise for energy storage applications. In this paper, nitrogen-doped hierarchical porous carbon (NPC) materials were synthesized by one-step carbonization process using agar as the carbon precursor, urea as the nitrogen precursor, and $KHCO_3$ as the activating agent. Owing to the combined influence of substantial nitrogen and oxygen functional groups, interconnected hierarchical porous structure and large specific surface area, the NPC-600 electrode delivers a high specific capacitance of 450 F g^{-1} and remarkable cyclic stability. Moreover, the NPC-600//NPC-600 symmetrical supercapacitor delivers an energy density of 29.41 Wh kg^{-1} and good cyclic performance. More interestingly, a zinc ion hybrid capacitor (ZIHC) constructed with NPC-600 as the positive electrode achieves a capacitance of 368.78 F g^{-1} (163.9 mAh g^{-1}), an energy density reaching 120.75 Wh kg^{-1} and superior cyclic characteristics. The research affords a straightforward way for fabricating heteroatom-doped porous carbon as electrode for supercapacitor and ZIHCs.

Keywords: Hierarchical porous carbon; $KHCO_3$; Agar; Supercapacitor; Zinc ion hybrid capacitor.

1 Introduction

Currently, electrochemical energy storage systems are deemed to hold significant potential for large-scale storage of electrical energy generated by renewable and sustainable energy sources.[1,2] Developing high-performance energy storage equipment (EES) is the general trend to deal with the unbalanced geographical distribution of most energy resources and the intermittent production of renewable energy like solar and wind power.[3] Many kinds of EES have been formulated, including lithium ion batteries (LIBs), water-based zinc ion batteries (ZIBs), sodium ion batteries, supercapacitors and so on.[4] Few of them have excellent power density and energy density simultaneously.[5] Generally, LIBs and ZIBs possess high energy density, but inferior cycle stability and low power density.[6,7] Although supercapacitors show better power density and outstanding electrochemical stability, their energy density needs to be further improved.[8]

Zinc ion hybrid capacitors (ZIHCs) can adeptly combine the advantages of supercapacitors (outstanding electrochemical stability and superior power density) and zinc ion batteries (excellent energy density), which has attracted extensive attention in recent years.[9–11] Zinc foil anodes are considered as promising negative electrodes because of the great abundance of zinc metal on the earth (300 times larger than lithium), high theoretical volumetric capacity and gravimetric capacity (5851 mAh cm^{-3} and 820 mAh g^{-1}), appropriate potential (−0.76 V *vs.* standard hydrogen electrodes) and excellent stability in both air and H_2O.[12,13] Porous carbon materials show great potential as cathode materials for ZIHCs attributed to the affordable price, adjustable pore structure, elevated specific surface area and outstanding electrochemical robustness.[14,15] Due to the limitation of the electronic double-layer energy storage mechanism, the energy density of porous carbon-based ZIHCs still cannot satisfy the requirements for high energy density EES.[16]

Enhancing the electrochemical capabilities of porous carbon materials can be significantly achieved by designing hierarchical porous structure and regulating the pore structure.[17–19] Generally, micropores contribute to the physical adsorption of ions at the electrolyte/electrode interface, thus contributing to the energy storage.[20–22] Mesopores may provide high-speed channels for fast passage of ions, while macropores can serve as ion buffer pools and

[a] *College of Chemistry, Chemical Engineering and Resource Utilization, Northeast Forestry University, 26 Hexing Road, Harbin 150040, P. R. China. E-mail: wuxiaoliang90@163.com*
[b] *School of Pharmacy, Health Science Center, Xi'an Jiaotong University, Xi'an, Shaanxi 710049, PR China. E-mail: minghuizhang@xjtu.edu.cn*

† Electronic supplementary information (ESI) available. See DOI: https://doi.org/10.1039/d5im00044k

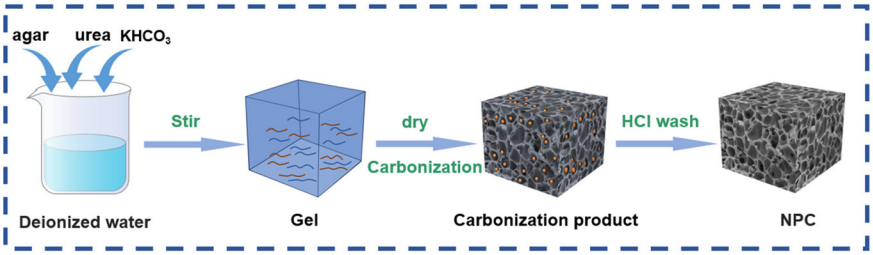

Fig. 1 Schematic illustration of the synthesis of NPC samples.

provide enough space for ion accommodation.[23] Furthermore, introducing heteroatom functional groups into carbon materials can promote the chemical adsorption of Zn^{2+} by introducing more electrochemical active sites, thus improving the charge storage capacity of positive carbon electrodes.[24,25] In particular, the nitrogen doping strategy can elevate the chemisorption of zinc ions on their surface, effectively enhancing the energy density of ZIHCs.[3]

Herein, we developed a single-step carbonization process to synthesize nitrogen-enriched hierarchical porous carbon (NPC) by utilizing agar as a carbon source, urea as a nitrogen source and $KHCO_3$ as an activator. Thanks to the combined influence of the significant nitrogen and oxygen functional group content, three-dimensional (3D) interconnected hierarchical porous structure and expansive specific surface area, the NPC-600 electrode delivers a specific capacitance of 450 F g^{-1} and superior cycle performance. Furthermore, the assembled NPC-600//NPC-600 symmetrical supercapacitor achieves an energy density of 29.41 Wh kg^{-1} and excellent cycle performance. Moreover, the ZIHC using NPC-600 as a cathode delivers a high capacitance of 368.78 F g^{-1} (163.9 mAh g^{-1}), an impressive energy density of 120.75 Wh kg^{-1} (100 W kg^{-1}), and exceptional cycle stability.

2 Results and discussion

The synthesis process of NPC materials is depicted in Fig. 1. Urea and potassium bicarbonate were dissolved in distilled

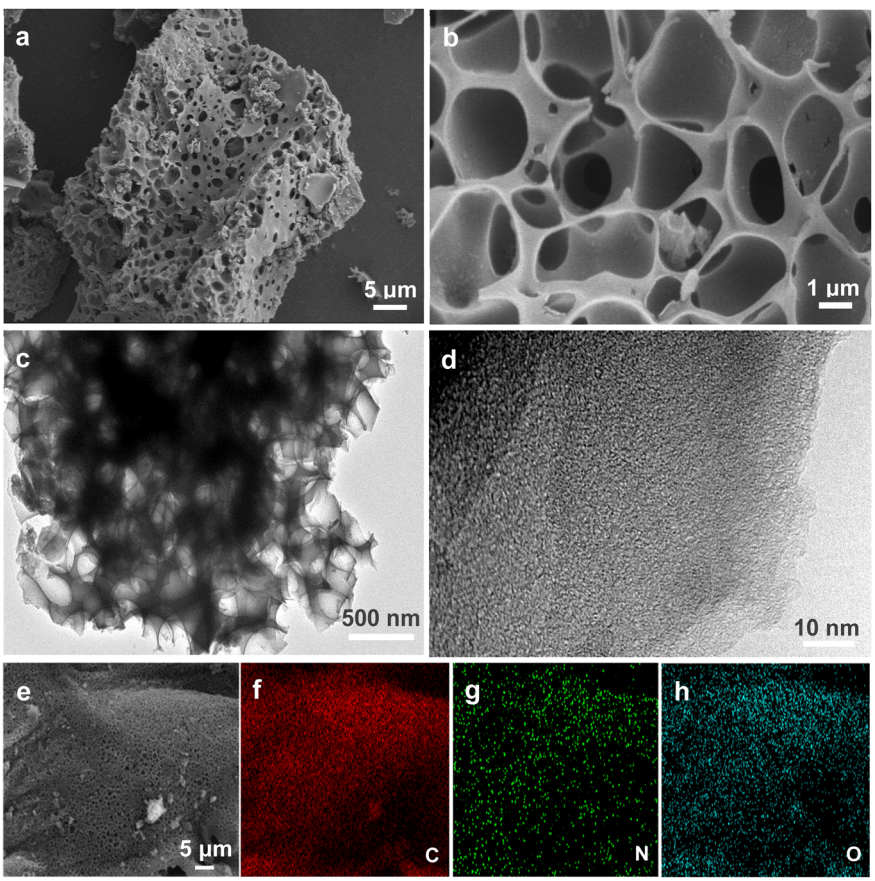

Fig. 2 (a and b) SEM images of NPC-600; (c) TEM image of NPC-600; (d) high resolution TEM image of NPC-600; (e) elemental mapping images of NPC-600: C (f), N (g) and O (h).

water with a certain proportion, and then agar powder was added, heated and stirred to form a gel. The obtained mixture is carbonized after freeze-drying, and washed with hydrochloric acid and distilled water to obtain porous carbon. The microstructure and morphology of the samples were examined using a scanning/transmission electron microscope (SEM/TEM). As illustrated in Fig. 2a and b, the NPC-600 specimens present a 3D porous skeleton with rich interconnected macropores. During the charging and discharging process, the 3D interconnected macropores facilitate rapid ion transfer within porous carbon. Furthermore, both NPC-500 (Fig. S1a†) and NPC-700 (Fig. S1b†) present a 3D interconnected porous framework containing numerous macropores. Significantly, as the carbonization temperature rises, the macropore size gradually increases. As illustrated in Fig. 2c, the TEM image of NPC-600 provides further confirmation of a 3D porous carbon skeleton. This fully demonstrates the dual activation of $KHCO_3$ (ref. 26–28) with urea[29] by the following mechanism. The possible chemical reactions that may occur are shown in eqn (1)–(6):

$$2KHCO_3 \rightarrow K_2CO_3 + CO_2 + H_2O \quad (1)$$

$$K_2CO_3 + C \rightarrow K_2O + 2CO \quad (2)$$

$$K_2CO_3 \rightarrow K_2O + CO_2 \quad (3)$$

$$K_2O + C \rightarrow 2K + CO \quad (4)$$

$$CO_2 + C \rightarrow 2CO \quad (5)$$

$$CO(NH_2)_2 \rightarrow NH_3 + HCNO \quad (6)$$

Moreover, the high-resolution TEM image proves the presence of numerous micropores on the carbon material surface, which is beneficial for energy storage applications. As illustrated in Fig. 2e and f, the carbon, oxygen and nitrogen elements are uniformly scattered in the carbon framework from the element mapping image of NPC-600.

An X-ray diffractometer (XRD) was employed to test the crystallographic structure of the specimens. As illustrated in Fig. 3a, all samples exhibit two broad and faint peaks at around 24.6° and 43.1°, corresponding to the (002) and (100) crystal planes of carbon materials. These two broad and faint peaks confirm that there are massive disordered porous structures in carbon samples. In addition, with the rise in temperature, the peak's intensity diminishes, attributed to the elevated temperatures favoring the activation and formation of a more disordered porous structure. The disordered porous structure was further evaluated by Raman. As shown in Fig. 3b, the I_D/I_G values of NPC-500, NPC-600 and NPC-700 are 0.9394, 0.9647 and 0.9920, respectively, which indicates that as the temperature increases, more disordered porous structures are generated, aligning closely with the XRD findings.[30–32] Furthermore, the moderate I_D/I_G value also indicates that NPC-600 has suitable disordered structures.

The material constituents and surface elements of the NPCs were examined *via* X-ray photoelectron spectroscopy (XPS). Fig. 4a displays three distinct peaks at 284.7 eV, 400.1 eV, and 531.9 eV, corresponding to C 1s, N 1s, and O 1s, respectively. The elemental analysis of NPC-600 indicates that the proportions of N and O are 5.30 at% and 10.65 at%. As illustrated in Fig. 4b, the C 1s spectrum with high resolution reveals four distinct peaks at 283.74 eV, 284.8 eV, 285.71 eV, and 287.05 eV, assigned to C–C, C–N, C–O, and C═O linkages, respectively. Fig. 4c presents the high-resolution N 1s spectrum with four peaks, which are attributed to pyridine N at 398.08 eV, pyrrole N at 399.48 eV, graphite N at 400.88 eV, and pyridine N oxide at 402.73 eV. Among these, N-6 and N-5 can produce pseudo-capacitance *via* the Faraday reaction, and N-*Q* adds two electrons to the conductive π system, increasing the prepared sample's conductivity.[33,34] As illustrated in Fig. 4d, the binding energies of the three peaks in the O 1s spectrum: C═O, C–O and O═C–O are 530.27 eV, 531.41 eV and 532.43 eV, respectively. The trends of the elemental composition values of carbon, nitrogen and oxygen in each NPC sample varying with temperature are shown in Table S1.† It can be seen from

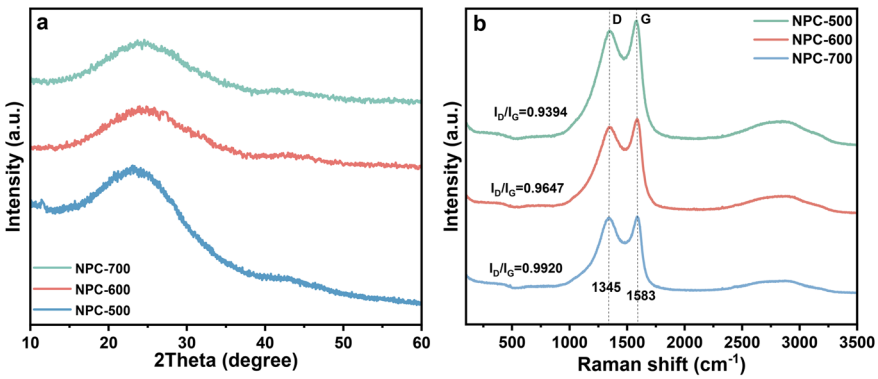

Fig. 3 (a) XRD patterns of NPC-500, NPC-600 and NPC-700; (b) Raman spectra of NPC-500, NPC-600 and NPC-700.

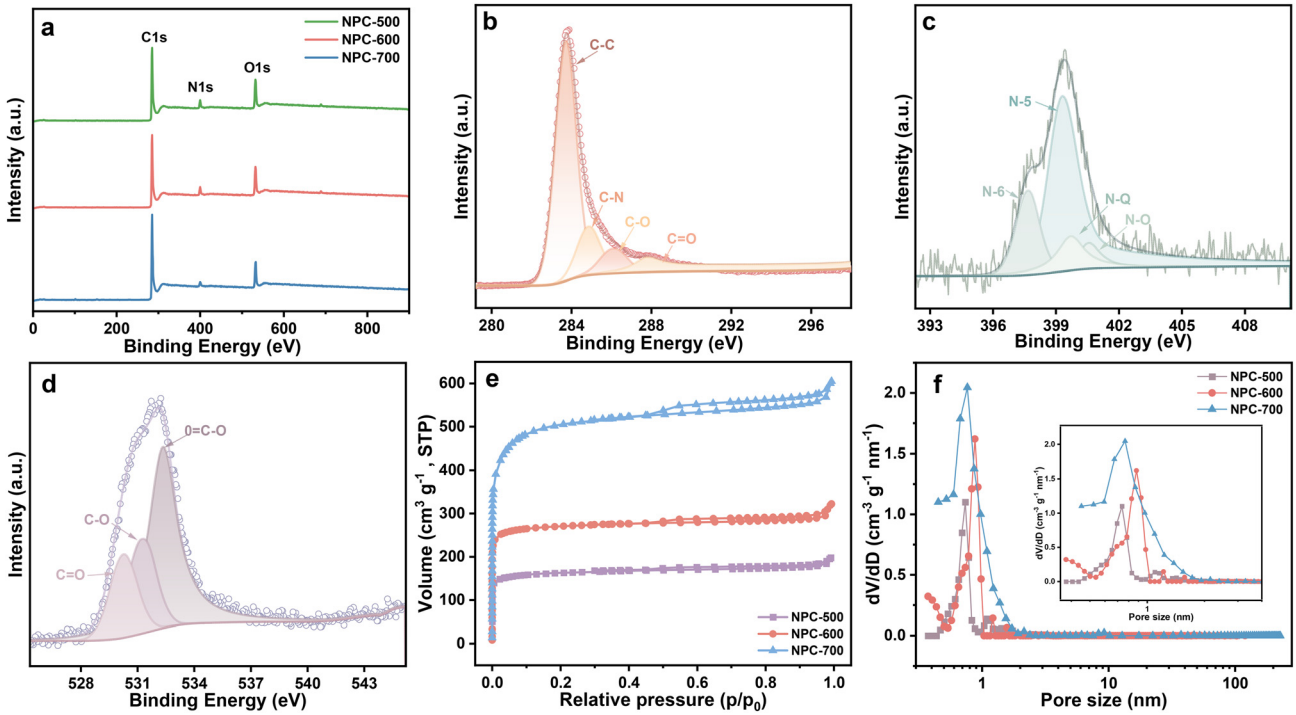

Fig. 4 (a) XPS survey spectra of NPC samples; high-resolution (b) C 1s, (c) N 1s and (d) O 1s spectra of the NPC-600 sample; (e) N_2 adsorption/desorption isotherms of NPC-500, NPC-600 and NPC-700; (f) pore size distribution curves of NPC-500, NPC-600 and NPC-700 (pore size concentrated distribution area of NPCs as the inset).

the table that the content of carbon atoms increases gradually with the increase of temperature, while the content of nitrogen atoms and oxygen atoms decreases gradually with the increase of temperature. From the percentage change trend of each element with temperature shown in Table S2,† it can be seen that the proportions of N-6 and N-5 in NPC-600 are 66.27% and 22.90%, respectively, which are higher than those in the other two samples. N-6 and N-5 are the main contributors to providing pseudo-capacitance, indicating that the introduction of N atoms has a remarkable effect. The presence of heteroatoms in the carbon material surface can not only significantly improve their wettability, but also participate in the redox reaction (Fig. S2†), providing additional pseudo-capacitance.

Nitrogen adsorption–desorption isotherm was employed to analyze the porosity of the carbon specimens. As illustrated in Fig. 4e, the three isotherms are similar in shape, aligning with the characteristic type I and type IV binding curves. In addition, under low relative pressure ($P/P_0 < 0.01$), sudden increase in pressure and high relative pressure ($P/P_0 > 0.45$) present a distinct hysteresis loop, which proves that micropores and mesopores/macropores exist in the samples. Table 1 illustrates the detailed surface area and pore structure parameters of the NPC specimens. As the temperature increases, the specific surface area of the NPC specimens enhances from 631.76 $m^2\ g^{-1}$ (NPC-500), climbing up to 1056.2 $m^2\ g^{-1}$ (NPC-600), and reaching 1890.1 $m^2\ g^{-1}$ (NPC-700). Through the application of density functional theory (DFT), the material's pore size distribution was determined. The NPC-600 sample displayed pore sizes falling within 0.8 nm to 1.1 nm, contributing favorably to energy storage (Fig. 4f).[29,31]

Cyclic voltammetry (CV), galvanostatic charge–discharge (GCD), as well as electrochemical impedance spectroscopy (EIS) analyses, were conducted in a 6 M KOH aqueous solution utilizing a three-electrode configuration to assess the electrochemical capabilities. As depicted in Fig. 5a, CV curves of the three electrodes at 50 mV s^{-1} are quasi-

Table 1 Porosity and yield parameters of the NPC carbon materials

Samples	S_{BET}[a] ($m^2\ g^{-1}$)	S_{mic}[b] ($m^2\ g^{-1}$)	S_{me}[c] ($m^2\ g^{-1}$)	S_{me}/S_{mic}	V_{total}[d] ($cm^3\ g^{-1}$)	D[e] (nm)
NPC-500	631.8	532.28	99.48	0.19	0.30	1.93
NPC-600	1056.2	901.36	154.84	0.17	0.49	1.86
NPC-700	1890.1	1471.30	418.80	0.29	0.93	1.96

[a] Specific surface area (S_{BET}) was calculated with a modified Brunauer–Emmett–Teller (BET) method. [b] Micropore surface area (S_{mic}) was obtained from the *t*-plot method. [c] Mesopore surface area (S_{me}) was obtained from the *t*-plot method. [d] Total pore volume (V_{total}) was estimated from the adsorbed amount at a relative pressure of 0.99. [e] Average pore diameter (D) was obtained from $D = 4V_{total}/S_{BET}$.

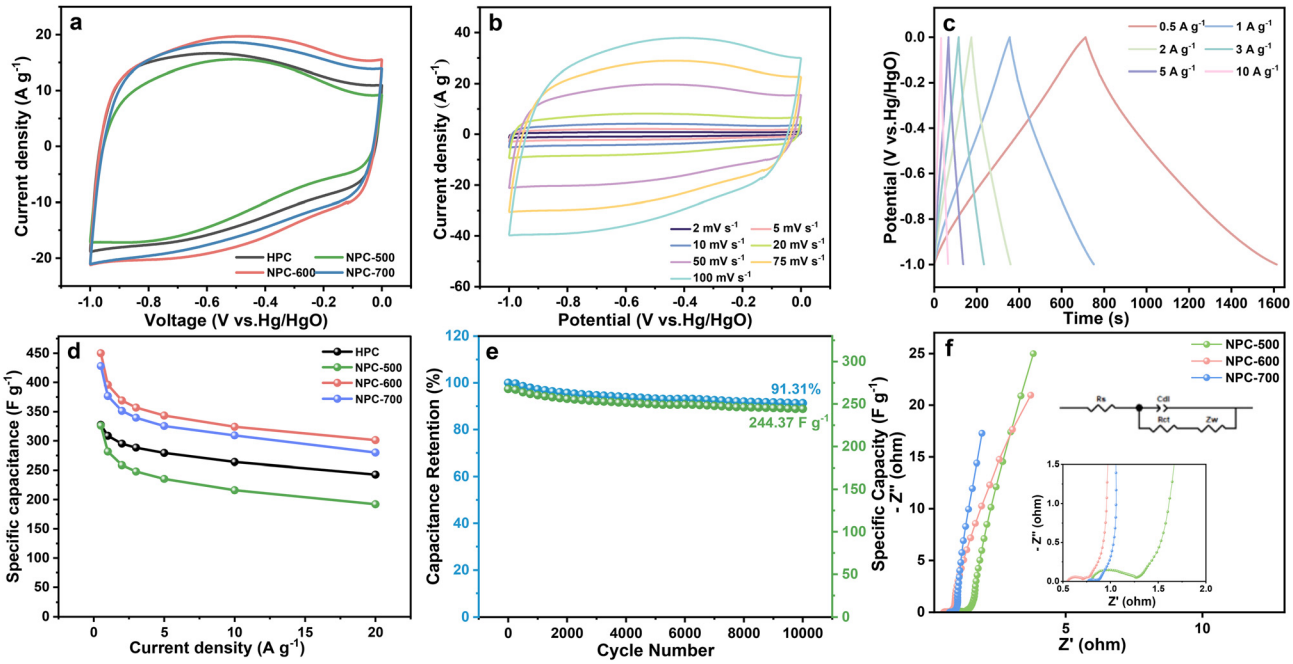

Fig. 5 (a) CV curves of HPC and NPC samples in different voltage ranges at 50 mV s^{-1}; (b) CV curves of NPC-600 at various scan rates; (c) GCD curves of NPC-600 at different current densities; (d) specific capacitance of HPC and NPC samples; (e) electrochemical stability of NPC-600 for 10 000 cycles tested at 200 mV s^{-1}; (f) Nyquist plot with an enlarged view of the high frequency region as the inset of NPCs samples.

rectangular shapes with faradaic humps, meaning that partial capacity comes from the contribution of Faraday pseudo-capacitance. Moreover, the NPC-600 electrode exhibits the biggest integration area, corresponding to the highest specific capacitance. As illustrated in Fig. S3,† consistent with the CV results, the NPC-600 electrode displays the longest discharge time, implying superior specific capacitance. As illustrated in Fig. 5b, when the scanning rate increases to 100 mV s^{-1}, the CV curve of the NPC-600 electrode still keeps a quasi-rectangular shape, demonstrating superior rate characteristic. According to the discharge time (Fig. 5c), the NPC-600 electrode achieves a specific capacitance of 450 F g^{-1} at 0.5 A g^{-1}, outperforming NPC-500 (326 F g^{-1}) and NPC-700 (428 F g^{-1}) and other reported porous carbon in the literature (Fig. 5d). At the same time, as illustrated in Fig. 5e, after 10 000 cycles at 200 mV s^{-1}, NPC-600 shows a capacitance retention rate of 91.31% (244.57 F g^{-1}), suggesting superior cyclic stability. The Nyquist diagrams of the NPC-600 electrode shows a small semicircle alongside a steep line, exhibiting a phase angle near 90° within the low frequency zone. Moreover, in the high frequency zone, the semicircle's center and the center shift away from the real axis (Fig. 5f). In the equivalent circuit, the value of solution resistance (R_s) is ascertained by the point where the curve meets the real axis at the upper frequency limit, which represents the equivalent series internal resistance related to electrode materials, contacts and electrolytes, and the value of charge transfer resistance (R_{ct}) is identified by the radius of the distorted semicircle observed in the high frequency domain, denoting the resistance to charge transfer pertinent to the Faraday redox reaction. The R_s and R_{ct} of NPC-600 are 0.55 Ω and 0.16 Ω, respectively, indicating good conductivity and a fast ion diffusion rate. In addition, we also tested the hydrogen evolution reaction (HER) electrocatalytic activity in a three-electrode system. The linear sweep voltammetry (LSV) map showed that NPC-600 showed good HER activity (Fig. S4a†). The linear fitting of the Tafel curve is carried out by the following Tafel equation (Fig. S4b†), and the Tafel slope of NPC-600 is 389 mV per decade, which further illustrates the good HER dynamics.

The NPC-600//NPC-600 symmetrical supercapacitor was constructed in 2 M $ZnSO_4$ aqueous solution. The CV analysis was performed at 50 mV s^{-1} to determine the optimized voltage testing range. The CV curve of the NPC-600//NPC-600 symmetrical supercapacitor maintained its integrity even at the voltage range of 0–1.8 V, showing no obvious deformation (Fig. 6a). Thus, the working voltage range is determined as the voltage range from 0 up to 1.8 V. As depicted in Fig. 6b, the CV measurements for the NPC-600//NPC-600 symmetrical supercapacitor span from 2 mV s^{-1} to 100 mV s^{-1}. Along with the scanning rate increasing, the CV curve shows no obvious deformation, indicating excellent rate behavior. Fig. 6c depicts the GCD plots for the NPC-600//NPC-600 symmetric supercapacitor under diverse current densities. By evaluating the discharge durations, the specific capacitance for the symmetric supercapacitor was estimated. As illustrated in Fig. 6d, the NPC-600//NPC-600 symmetric supercapacitor achieves a specific capacitance of 65.37 F g^{-1} at a current density of 0.25 A g^{-1}. As illustrated in Fig. 6e, the NPC-600//NPC-600 symmetrical supercapacitor boasts an impressive energy density of 29.41 Wh kg^{-1} (300 W kg^{-1}) thanks to its extensive voltage window and elevated specific capacitance,

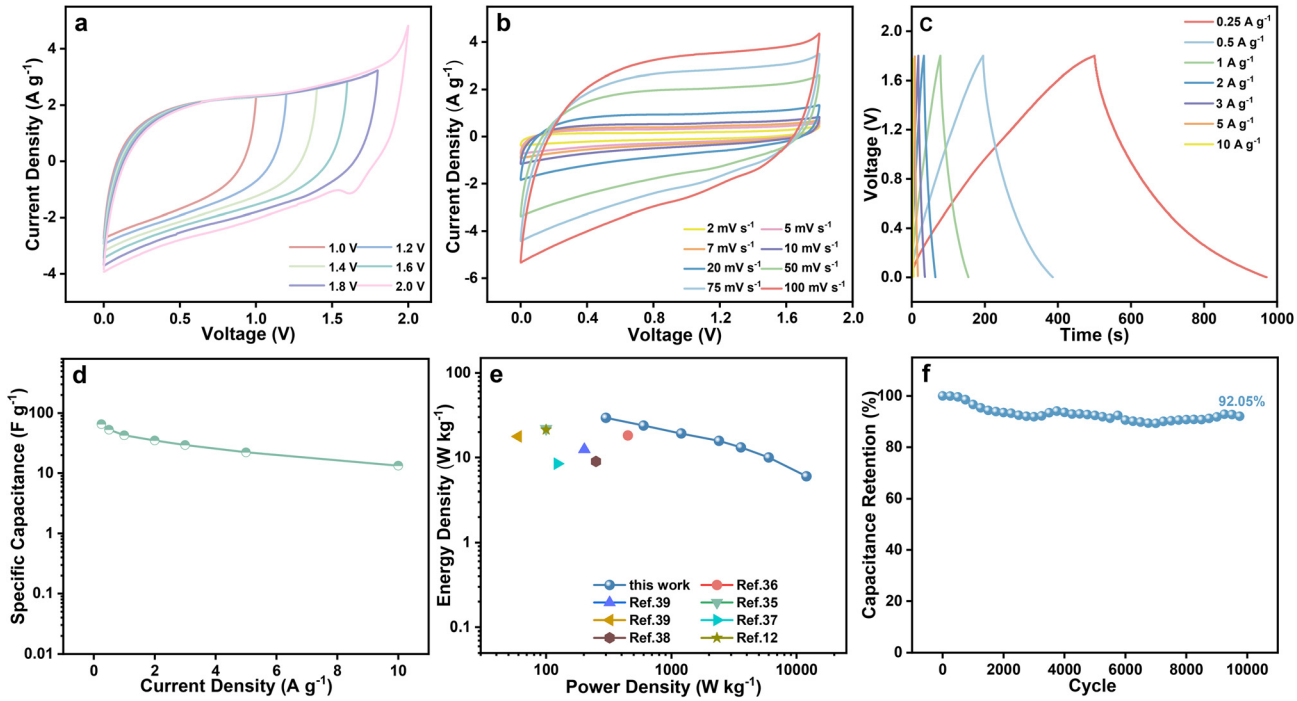

Fig. 6 (a) CV curves of the NPC-600//NPC-600 symmetrical supercapacitor in different voltage ranges at 50 mV s^{-1}; (b) CV curves of the NPC-600//NPC-600 symmetrical supercapacitor at various scan rates; (c) GCD curves of the NPC-600//NPC-600 symmetrical supercapacitor at different current densities; (d) specific capacitance of the NPC-600//NPC-600 symmetrical supercapacitor; (e) Ragone plots of the NPC-600//NPC-600 symmetrical supercapacitor; (f) electrochemical stability of the NPC-600//NPC-600 symmetrical supercapacitor for 10 000 cycles tested at 200 mV s^{-1}.

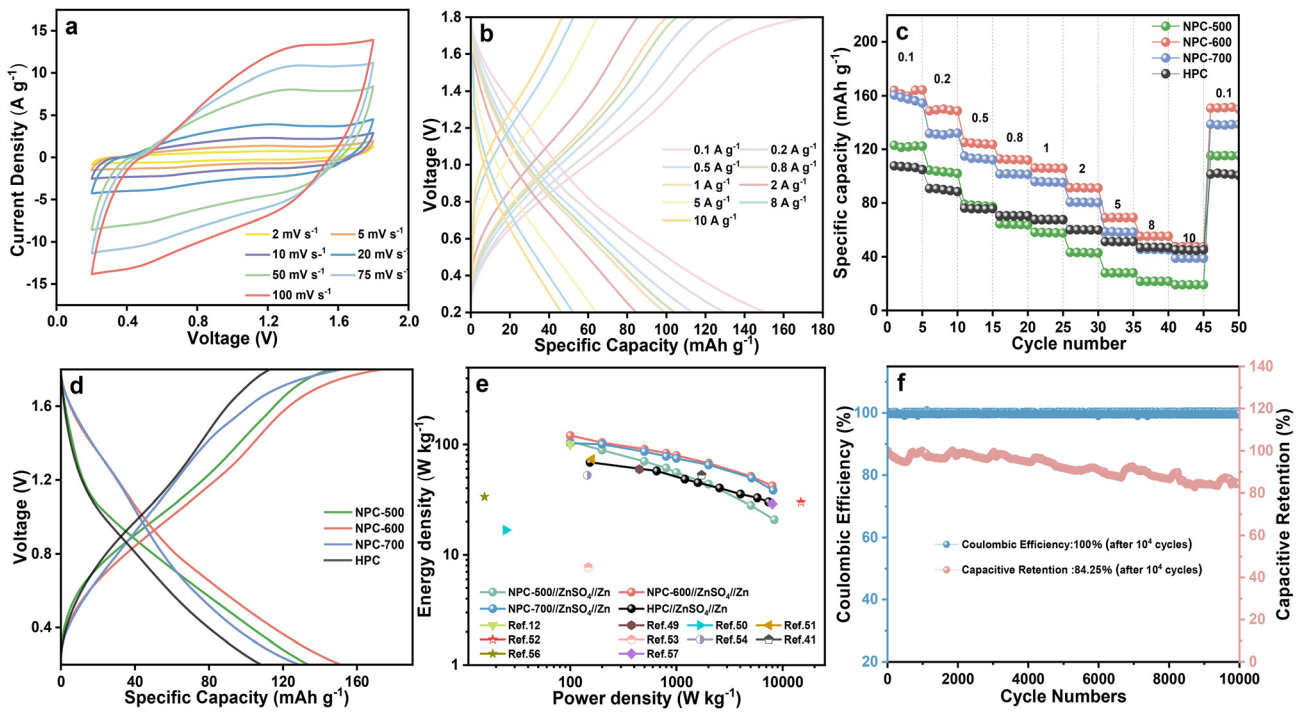

Fig. 7 The electrochemical properties of ZIHCs based on the NPC cathode: (a) CV curves of the Zn//$ZnSO_4$//NPC-600 hybrid capacitor at various scan rates; (b) GCD curves of the Zn//$ZnSO_4$//NPC-600 hybrid capacitor at various current densities; (c) cyclic performance of specific capacitance at various current densities; (d) CV curves of the Zn//$ZnSO_4$//NPC hybrid capacitor at 0.1 A g^{-1}; (e) Ragone plots of the Zn//$ZnSO_4$//NPC-600 hybrid capacitor; (f) electrochemical stability of the Zn//$ZnSO_4$//NPC-600 hybrid capacitor for 10 000 cycles.

which is higher than those reported in other documents.[12,35–40] As illustrated in Fig. 6f, the capacitance retention rate of the NPC-600//NPC-600 symmetrical supercapacitor is 92.05% after 10 000 cycles at a scanning rate of 200 mV s^{-1}, reflecting its excellent electrochemical performance.

A zinc ion hybrid capacitor utilizing NPC-600 as the cathode and zinc foil as the anode in 2 M $ZnSO_4$ solution was constructed to assess the electrochemical characteristics of the electrode materials in practical applications. As illustrated in Fig. 7a, the CV graphs exhibit a rectangular shape, and the redox peak is reversible, confirming that the ZIHC operates *via* a mechanism that encompasses both battery and supercapacitor characteristics.[41–46] Even at 100 mV s^{-1}, the rectangular shape will not change significantly, reflecting excellent rate behavior. As illustrated in Fig. 7b, the GCD plots for the Zn//$ZnSO_4$//NPC-600 hybrid capacitor maintain their form as the current density escalates, demonstrating consistent reversibility. However, in the Nyquist diagram of ZIHC (Fig. S5†), a prominently deformed semicircle and a distinct line with a gradient below 1 in the high frequency range are observed, signifying a high R_{ct} value and a notable ion diffusion resistance. This is not only related to the poor diffusion of hydrated Zn^{2+} and the planar structure on the surface of the zinc foil electrode, but also related to the inefficient Zn^{2+} plating/stripping processes and kinetics.[47,48]

Fig. 7c shows a comparison chart of ZIHC capacitance attenuation. It has been computed that the peak specific capacitance for ZIHC utilizing NPC-600 as the cathode material can hit 368.78 F g^{-1} (163.9 mAh g^{-1}) when subjected to 0.1 A g^{-1}. Concurrently, for ZIHC systems with NPC-500 and NPC-700 cathodes, their respective maximum specific capacitance values are 276.75 F g^{-1} (123 mAh g^{-1}) and 360.9 F g^{-1} (160.4 mAh g^{-1}). Notably, the Zn//$ZnSO_4$//NPC-600 hybrid capacitor is capable of sustaining a capacitance level of 106.88 F g^{-1} (47.5 mAh g^{-1}) even at 10 A g^{-1}, highlighting its superior charge–discharge attributes. Fig. 7d illustrates the GCD profiles of the ZIHC based on different NPC cathodes of 0.1 A g^{-1}, and it is found that the specific capacitance of the Zn//$ZnSO_4$//NPC-600 hybrid capacitor is the highest among the three. At the same time, it also validates the hybrid energy storage mechanism that the curve deviates from the standard symmetrical linear shape. In Fig. 7e, the ZIHC with NPC-600 as the cathode can reach an impressive energy density of 120.75 Wh kg^{-1} (100 W kg^{-1}), surpassing previously documented ZIHC values.[12,41,49–56] The cycle stability of the Zn//$ZnSO_4$//NPC-600 hybrid capacitor was tested at 5 A g^{-1}, where it retained 84.25% of its initial value after 10 000 cycles (Fig. 7f), showing outstanding cycling performance.

Through the computation of the distinct charge storage processes' contributions to the overall capacitance and examination of the CV curve's electrochemical dynamics, the electrochemical activity of the NPC-600 cathode in a hybrid capacitor was initially grasped. The CV test was carried out over a scanning rate range from 5 mV s^{-1} to 100 mV s^{-1}, and the non-rectangular CV profile can indicate the mixed charge storage mechanism (Fig. S7†). Upon setting the scanning rate to 5 mV s^{-1}, about 67.97% of NPC-600's total current was governed by diffusion control, as indicated by the purple shaded area. In general, two formulas are applicable for assessing the current response across varying voltages:[12]

$$i = av^b \quad (1)$$

$$\log(i) = b \times \log(v) + \log(a) \quad (2)$$

In adherence to the mentioned formula, when the value of b hovers around 0.5, it signifies that the electrochemical reaction is predominantly governed by diffusion. Conversely, when b tends towards 1, it suggests that a capacitive reaction is at play. As indicated by the reduction process data, the computed value of b is 0.75 (refer to Fig. 8a), suggesting that the charge storage mechanism in the zinc ion hybrid capacitor, utilizing NPC-600 as the cathode, is primarily dominated by capacitance and diffusion. Notably, the calculated values of b for the other samples are 0.71 and 0.89, respectively (Fig. S6a†), which indicates that the charge storage mechanism in zinc ion hybrid capacitors using them as cathodes is also mainly controlled by capacitance and diffusion. Moreover, the following formula can be used to quantitatively calculate the current response at a given

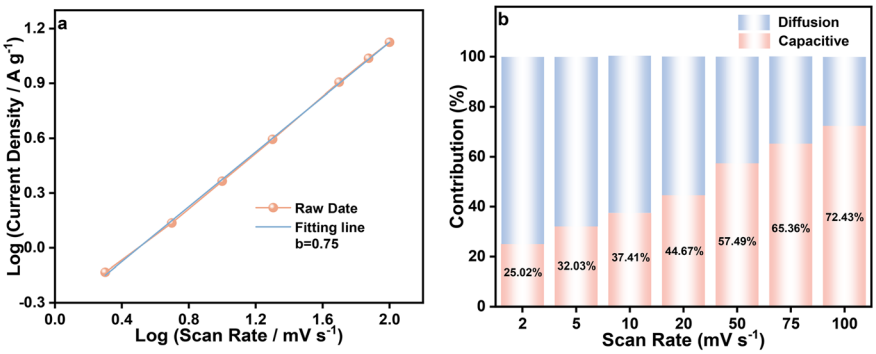

Fig. 8 (a) The b-value obtained from the linear relationship between log(i) and log(v); (b) the percentage of capacitive contributions at different scan rates of the Zn//$ZnSO_4$//NPC-600 hybrid capacitor.

voltage: $i = k_1v + k_2v^{1/2}$, where k_1v and $k_2v^{1/2}$ respectively represent the capacitance and diffusion control process. Based on the formula, the current response contribution rate is calculated. As illustrated in Fig. 8b, the capacitance contribution ratio exhibits a direct correlation with the scanning rate. At slower scanning rates, diffusion plays a dominant role in the contribution. As the scanning rate rises, the diffusion contribution percentage steadily diminishes, and concurrently, the capacitance behavior contribution percentage, thereby confirming that the NPC-600 cathode in the ZIHC operates with a hybrid control mechanism for energy storage. The data for different scanning rates are illustrated in Fig. S7.† As the scanning rate escalates to 100 mV s^{-1}, the percentage of capacitance contribution also increased to 72.43%, which proves that the NPC-600 electrode has a fast dynamic process and capacitance control behavior at a fast scanning rate. These findings suggest that ions tend to be accommodated near the electrode surface during the reaction, helping to prevent the degradation of the electrode material's structure. Furthermore, the capacitance reaction process efficiently reduces the electrolyte ion transmission route, thereby enhancing the rate capability of the electrode and boosting the overall functionality of electrochemical energy storage systems. The exceptional performance of NPC-600 can be credited to its distinct stratified porosity configuration, as well as the contribution of the N and O functional groups.

3 Conclusion

In summary, we have synthesized nitrogen-doped hierarchical porous carbon through a one-step carbonization process using a mixture of agar, urea, and $KHCO_3$. Owing to the combined influence of the substantial nitrogen and oxygen functional groups, the 3D interconnected porous framework, and the expansive specific surface area, the NPC-600 electrode exhibits a notable specific capacitance of 450 F g^{-1} along with superior cyclic stability. Moreover, the NPC-600//NPC-600 symmetrical supercapacitor delivers an energy density of 29.41 Wh kg^{-1} and maintains exceptional cyclic performance. Furthermore, the ZIHC, consisting of NPC-600 serving as the cathode and zinc foil as the anode, achieves a notable capacitance of 368.78 F g^{-1} (163.9 mAh g^{-1}) and an impressive energy density reaching 120.75 Wh kg^{-1} (100 W kg^{-1}), and exhibits exceptional cycle stability in 2 M $ZnSO_4$ electrolyte solution.

4 Experimental section

Urea (2 g) and potassium bicarbonate (2 g) were dissolved in 20 mL distilled water. Subsequently, 2 g agar was introduced, thoroughly stirred, and heated until it gelled. Then, the gel was placed in the refrigerator until completely frozen, then it was freeze dried in a freeze dryer. The sample was heated to various temperatures (600 °C, 700 °C, 800 °C) at a heating pace of 5 °C min^{-1} in N_2, respectively, and then carbonized and activated for 120 min. After acid washing and water washing, the carbonized material was dried to obtain the resultant sample, which was named NPC-*X*, where *X* stands for temperature. In the ESI,† comprehensive characterization techniques and electrochemical approaches are presented.

Data availability

The authors declare that the data supporting the findings of this study are available within the paper and its ESI† files. Should any raw data files be needed in another format they are available from the corresponding author upon reasonable request. Source data are provided with this paper.

Conflicts of interest

The authors declare no conflict of interest.

Acknowledgements

This work was supported by the Natural Science Foundation Funded Project of Heilongjiang Province (YQ2023E002).

References

1 Y. Wang, S. Sun, X. Wu, H. Liang and W. Zhang, Status and opportunities of zinc ion hybrid capacitors: Focus on carbon materials, current collectors, and separators, *Nano-Micro Lett.*, 2023, **15**, 78.
2 D. Gao, Z. Luo, C. Liu and S. Fan, A survey of hybrid energy devices based on supercapacitors, *Green Energy Environ.*, 2023, **8**, 972.
3 H. Zhang, Q. Liu, Y. Fang, C. Teng, X. Liu, P. Fang, Y. Tong and X. Lu, Boosting Zn-ion energy storage capability of hierarchically porous carbon by promoting chemical adsorption, *Adv. Mater.*, 2019, **31**, 1904948.
4 J. Chen, T. Song, M. Sun, S. Qi, C. Chen, Y. Zhao and X. Wu, Cobalt nickel selenide with MXene and graphene dual support system to enhance electrochemical activity and stability for supercapacitors, *J. Alloys Compd.*, 2024, **1009**, 176786.
5 H. Li, W. Shi, L. Liu, X. Zhang, P. Zhang, Q. Wang, Y. Liu, Z. Wang and J. Dou, Coupling effect of vacancy defects and multi-adsorption sites in porous carbon cathode for high-performance aqueous zinc-ion hybrid capacitors, *Chem. Eng. J.*, 2024, **487**, 150630.
6 L. Liu, Z. Sun, Y. Lu, J. Zhang, Y. Li, G. Zhang, X. Chen, S. Omanovic, S. Sun and H. Song, d-Calcium pantothenate-derived porous carbon: carbonization mechanism and application in aqueous Zn-ion hybrid capacitors, *J. Mater. Chem. A*, 2023, **11**, 14311.
7 M. S. Javed, T. Najam, I. Hussain, M. Idrees, A. Ahmad, M. Imran, S. S. A. Shah, R. Luque and W. Han, Fundamentals and scientific challenges in structural design of cathode materials for zinc-ion hybrid supercapacitors, *Adv. Energy Mater.*, 2023, **13**, 2202303.

8 M. Gao, Y. Chen, W. Xiao, L. Miao, H. Kong, W. Liang, T. Ao, H. Mou and W. Chen, Elucidating the efficacious capacitive deionization defluorination behaviors of heteroatom-doped hierarchical porous carbon nanofibers membrane, *Sep. Purif. Technol.*, 2025, **359**, 130803.
9 Q. Chu, Z. Chen, C. Cui, Y. Zhang, X. Li, Y. Xu, Y. Li, H. Yang, Y. Cui and Q. Liu, Engineering C O groups in 3D hollow porous carbon for boosting Zn-ion hybrid supercapacitors, *J. Energy Storage*, 2024, **98**, 113065.
10 B. Yang, W. Zhao, Z. Gao, J. Yang, W. Shi, Y. Zhang, Q. Su, B. Xu and G. Du, Flexible CNT@porous carbon sponge cathode with large mesopores for high-rate zinc-ion hybrid capacitors, *Carbon*, 2024, **218**, 118695.
11 F. Zhang, H. Lang, J. Wu and J. Huang, Sorghum-derived porous carbon for outstanding green supercapacitors, *New J. Chem.*, 2024, **48**, 332–341.
12 F. Mo, Y. Wang, T. Song and X. Wu, Nitrogen and oxygen co-doped hierarchical porous carbon for zinc-ion hybrid capacitor, *J. Energy Storage*, 2023, **72**, 108228.
13 T. Song, Y. Zhao, C. Chen, X. Gui, X. Wu and X. Wang, Recyclable NaCl template assisted preparation of N/O co-doped porous carbon for zinc-ion hybrid capacitor, *J. Energy Storage*, 2024, **98**, 113148.
14 T. Li, D. Wang, P. Ding, H. Li, H. Huang, X. Liu, T. Wang, Q. Pei, X. Liu and R. Guo, Highly tri-heteroatom doped porous carbon for aqueous and flexible quasi-solid-state zinc-ion hybrid supercapacitors, *J. Energy Storage*, 2024, **89**, 111789.
15 F. Ji, S. Gou, J. Tang, Y. Xu, S. M. Eldin, W. Mai, J. Li and B. Liu, High-performance Zn-ion hybrid supercapacitor enabled by a lightweight polyimide-based anode, *Chem. Eng. J.*, 2023, **474**, 145786.
16 R. Bahadur, B. Wijerathne and A. Vinu, Multiple heteroatom doped nanoporous biocarbon for supercapacitor and zinc-ion capacitor, *ChemSusChem*, 2024, **17**, e202400999.
17 J. He, G. Peng, Y. Wei, Y. Zhu, L. Jiang and X. He, N/S co-doped interconnected hierarchical porous carbon cathode for zinc-ion hybrid capacitors with high energy density, *J. Power Sources*, 2024, **613**, 234937.
18 D. Xie, S. Liu, W. Wei, Z. Zhou, X. Fu, Z. Shang, Y. Wang and S. Yuan, Nitrogen-doped porous carbon fiber as a self-supporting electrode for boosting zinc-ion hybrid supercapacitors, *Ind. Eng. Chem. Res.*, 2024, **63**, 21146.
19 W. M. Nasution, A. Apriwandi, R. Dewi, J. G. Manjunatha, A. Fudholi, N. Chitraningrum, R. Taslim and E. Taer, O-and Zn-self-dual-doped porous carbon derived from fruit waste for boosting supercapacitor performance, *Int. J. Energy Clean Environ.*, 2025, **26**, 35.
20 Q. Liu, D. Wu, T. Wang and Y. Guo, Polysaccharide of agar based ultra-high specific surface area porous carbon for superior supercapacitor, *Int. J. Biol. Macromol.*, 2023, **228**, 40.
21 X. Zhang, C. Jiang, J. Zhao, B. Liu, T. Wang, H. Li, W. Shi, X. Zhao, X. Yan and Y. Liu, Porous and graphitic carbon nanosheets with controllable structure for zinc-ion hybrid capacitor, *J. Colloid Interface Sci.*, 2024, **664**, 146.
22 Y. Liu and L. Wu, Recent advances of cathode materials for zinc-ion hybrid capacitors, *Nano Energy*, 2023, **109**, 108290.
23 F. Wen, Y. Yan, S. Sun, X. Li, X. He, Q. Meng, J. Zhe Liu, X. Qiu and W. Zhang, Synergistic effect of nitrogen and oxygen dopants in 3D hierarchical porous carbon cathodes for ultra-fast zinc ion hybrid supercapacitors, *J. Colloid Interface Sci.*, 2023, **640**, 1029.
24 Y. Lv, L. Zhang, X. Wei, B. Qiu, W. Zhang, Q. Qin, D. Jia, X. He, Z. Liu and F. Wei, The emerging of zinc-ion hybrid supercapacitors: Advances, challenges, and future perspectives, *Sustainable Mater. Technol.*, 2023, **35**, e00536.
25 D. Jia, Z. Shen, W. Zhou, Y. Li, J. He, L. Jiang, Y. Wei and X. He, Ultrahigh N-doped carbon with hierarchical porous structure derived from metal-organic framework for high-performance zinc ion hybrid capacitors, *Chem. Eng. J.*, 2024, **485**, 149820.
26 H. Qiang, M. Shi, Y. Pan, F. Wang and M. Xia, Sustainable pore expansion approach for the fabrication of nitrogen-doped porous carbon for capacitive deionization, *Sep. Purif. Technol.*, 2025, **361**, 131294.
27 M. Zhou, Y. Lin, H. Xia, X. Wei, Y. Yao, X. Wang and Z. Wu, A molecular foaming and activation strategy to porous N-doped carbon foams for supercapacitors and CO_2 capture, *Nano-Micro Lett.*, 2020, **12**, 58.
28 J. Shi, H. Cui, J. Xu and N. Yan, Carbon spheres synthesized from $KHCO_3$ activation of glucose derived hydrochar with excellent CO_2 capture capabilities at both low and high pressures, *Sep. Purif. Technol.*, 2022, **294**, 121193.
29 B. Xue, C. Liu, X. Wang, Y. Feng, J. Xu, F. Gong and R. Xiao, Urea-boosted gas-exfoliation synthesis of lignin-derived porous carbon for zinc ion hybrid supercapacitors, *Chem. Eng. J.*, 2024, **480**, 147994.
30 J. Chen, H. Wei, H. Chen, W. Yao, H. Lin and S. Han, N/P co-doped hierarchical porous carbon materials for superior performance supercapacitors, *Electrochim. Acta*, 2018, **271**, 49.
31 J. Qiao, J. Zhang, W. Geng, S. Wang and F. Wei, N doped porous carbon derived from coal tar pitch for supercapacitor and zinc ion hybrid capacitor, *Ionics*, 2025, **31**, 6155.
32 C. Zhu, M. Wang, G. Yang, T. Lu and L. Pan, N, P dual-doped hollow carbon spheres for high-performance supercapacitors, *J. Solid State Electrochem.*, 2017, **21**, 3631.
33 F. Wei, Y. Wei, J. Wang, M. Han and Y. Lv, N, P dual doped foamy-like carbons with abundant defect sites for zinc ion hybrid capacitors, *Chem. Eng. J.*, 2022, **450**, 137919.
34 Y. Lu, Z. Li, Z. Bai, H. Mi, C. Ji, H. Pang, C. Yu and J. Qiu, High energy-power Zn-ion hybrid supercapacitors enabled by layered B/N co-doped carbon cathode, *Nano Energy*, 2019, **66**, 104132.
35 S. Zhang, Q. Zhang, R. Ma, X. Feng, F. Chen, D. Wang, B. Zhang, Y. Wang, N. Guo, M. Xu, L. Wang and D. Jia, Boosting the capacitive performance by constructing O, N co-doped hierarchical porous structure in carbon for supercapacitor, *J. Energy Storage*, 2024, **82**, 110569.
36 X. Han, H. Jiang, Y. Zhou, W. Hong, Y. Zhou, P. Gao, R. Ding and E. Liu, A high performance nitrogen-doped porous activated carbon for supercapacitor derived from pueraria, *J. Alloys Compd.*, 2018, **744**, 544.

37 X. Fu, J. Chang, W. Guo, T. Gu, Y. Liu, L. Chen, G. Wang and F. Bao, Heteroatoms-doped hierarchically porous graphene as electrode material for supercapacitors with ultra-high capacitance, *J. Power Sources*, 2024, **603**, 234474.
38 K. Pandey and H. K. Jeong, Coffee waste-derived porous carbon based flexible supercapacitors, *Chem. Phys. Lett.*, 2022, **809**, 140173.
39 F. Wei, H. Zhang, J. Wang, J. Zhuang and Y. Lv, N, S co-doped porous carbons with well-developed pores for supercapacitor and zinc ion hybrid capacitor, *J. Alloys Compd.*, 2022, **907**, 164536.
40 B. Xue, C. Liu, X. Wang, Y. Feng, J. Xu, F. Gong and R. Xiao, Urea-boosted gas-exfoliation synthesis of lignin-derived porous carbon for zinc ion hybrid supercapacitors, *Chem. Eng. J.*, 2024, **480**, 147994.
41 H. Wang, M. Wang and Y. Tang, A novel zinc-ion hybrid supercapacitor for long-life and low-cost energy storage applications, *Energy Storage Mater.*, 2018, **13**, 1.
42 X. Guo, Q. Peng, R. Yang, G. Cao, J. Wen, K. Shin, Y. Zheng, S. Tunmee, C. Zou, Y. Zheng, X. Zhou and Y. Tang, Non-coordinating charge transfer enables ultrafast desolvation of hydrated zinc ions in the outer Helmholtz layer for stable aqueous Zn metal batteries, *Natl. Sci. Rev.*, 2025, **12**, nwaf70.
43 C. Cui, H. Wang, M. Wang, X. Ou, Z. Wei, J. Ma and Y. Tang, Hollow carbon nanobelts codoped with nitrogen and sulfur *via* a self-templated method for a high-performance sodium-ion capacitor, *Small*, 2019, **15**, 1902659.
44 S. Li, J. Shang, M. Li, M. Xu, F. Zeng, H. Yin, Y. Tang, C. Han and H. M. Cheng, Design and synthesis of a π-conjugated N-heteroaromatic material for aqueous zinc-organic batteries with ultrahigh rate and extremely long life, *Adv. Mater.*, 2023, **35**, 2207115.
45 C. Chang, S. Hu, T. Li, F. Zeng, D. Wang, S. Guo, M. Xu, G. Liang, Y. Tang, H. Li, C. Han and H. Cheng, A robust gradient solid electrolyte interphase enables fast Zn dissolution and deposition dynamics, *Energy Environ. Sci.*, 2024, **17**, 680.
46 B. Ji, W. Yao and Y. Tang, High-performance rechargeable zinc-based dual-ion batteries, *Sustainable Energy Fuels*, 2020, **4**, 101.
47 Y. Liu, Y. Li, X. Huang, H. Cao, Q. Zheng, Y. Huo, J. Zhao, D. Lin and B. Xu, Copper hexacyanoferrate solid-state electrolyte protection layer on Zn metal anode for high-performance aqueous zinc-ion batteries, *Small*, 2022, **18**, 2203061.
48 Z. Luo, Y. Xia, S. Chen, X. Wu, E. Akinlabi, B. B. Xu, H. Pan, M. Yan and Y. Jiang, A homogeneous plating/stripping mode with fine grains for highly reversible Zn anodes, *Energy Environ. Sci.*, 2024, **17**, 6787.
49 S. Chen, L. Ma, K. Zhang, M. Kamruzzaman, C. Zhi and Juan Antonio Zapien, A flexible solid-state zinc ion hybrid supercapacitor based on co-polymer derived hollow carbon sphere, *J. Mater. Chem. A*, 2019, **7**, 7784.
50 G. Chen, B. Lu, J. Li, C. Wu, Y. Xiao, H. Dong, Y. Liang, Y. Liu, H. Hu and M. Zheng, Regulating medical wasted cotton into porous carbons for high-performance supercapacitors and zinc-ion hybrid capacitors, *J. Power Sources*, 2024, **599**, 234146.
51 S. Chen, G. Yang, X. Zhao, N. Wang, T. Luo, X. Chen, T. Wu, S. Jiang, P. A. van Aken, S. Qu, T. Li, L. Du, J. Zhang, H. Wang and H. Wang, Hollow mesoporous carbon spheres for high performance symmetrical and aqueous zinc-ion hybrid supercapacitor, *Front. Chem.*, 2020, **8**, 663.
52 L. Dong, X. Ma, Y. Li, L. Zhao, W. Liu, J. Cheng, C. Xu, B. Li, Q. Yang and F. Kang, Extremely safe, high-rate and ultralong-life zinc-ion hybrid supercapacitors, *Energy Storage Mater.*, 2018, **13**, 96.
53 Y. Fang, Q. Zhang, D. Zhang and L. Cui, The synthesis of porous carbons from a lignin-rich residue for high-performance supercapacitors, *Xinxing Tan Cailiao*, 2022, **37**, 743.
54 Z. Liu, G. Li, T. Cui, A. Borodin, C. Kuhl and F. Endres, A battery-supercapacitor hybrid device composed of metallic zinc, a biodegradable ionic liquid electrolyte and graphite, *J. Solid State Electrochem.*, 2018, **22**, 91.
55 F. Wei, H. Tian, P. Chen, Y. Lv and J. Huang, Construction of porous carbon nanosheets by dual-template strategy for zinc ion hybrid capacitor, *Appl. Surf. Sci.*, 2023, **613**, 156021.
56 L. Yao, J. Jiang, H. Peng, H. Yang, S. Liu, X. Wen, P. Cai, Y. Zou, H. Zhang, F. Xu, L. Sun and X. Lu, Glutinous rice-derived carbon material for high-performance zinc-ion hybrid supercapacitors, *J. Energy Storage*, 2023, **58**, 106378.